

Modeling the locomotion of articulated soft robots in granular medium

Journal Title
XX(X):1–13
©The Author(s) 2019
Reprints and permission:
sagepub.co.uk/journalsPermissions.nav
DOI: 10.1177/ToBeAssigned
www.sagepub.com/

SAGE

Yayun Du¹, Jacqueline Lam¹, Karunesh Sachanandani¹, and M. Khalid Jawed¹

Abstract

Soft robots, in contrast to their rigid counter parts, have infinite degrees of freedom that are coupled with their interaction with the environment. We consider the locomotion of an untethered robot, in the granular medium, comprised of multiple flexible flagella that rotate about an axis by a motor. Drag from the grains causes the flagella to deform and the deformed shape generates a net forward propulsion. This external drag force depends on the shape of the flagella, while the change in flagellar shape is the result of the competition between the external loading and elastic forces. We introduce a numerical tool that couples discrete differential geometry based simulation of elastic rods - our model for flagella - and a resistive force theory based model for the drag. In parallel with simulations, we conduct experiments to quantify the propulsive speed of this class of robots. We find reasonable quantitative agreement between experiments and simulations. Owing to a rod-based kinematic representation of the robot, the simulation runs faster than real-time, and, therefore, we can use it as a design tool for this class of soft robots. We find that there is an optimal rotational speed at which maximum efficiency is achieved. Moreover, both experiments and simulations show that increasing the number of flagella decreases the speed of the robot. We also gain insight into the mechanics of granular medium - while resistive force theory can successfully describe the propulsion at low number of flagella, it fails when more flagella are added to the robot.

Keywords

Soft robotics, biomimetics, locomotion, design and modeling, bacteria, flagella, discrete elastic rod, granular medium, resistive force theory

1 Introduction

Recent years have witnessed the expeditious growth of soft robots that can potentially work safely side by side with humans, reduce manufacturing costs, and revolutionize our ability to accomplish search and rescue missions (Majidi et al. 2013). In contrast to traditional machines and robots made of rigid skeletons or rigid materials, soft robots are primarily composed of intrinsically soft matter and fluids, enabling them to deform elastically into reversible shapes (Shepherd et al. 2011; Lin et al. 2011; Kim et al. 2013; Tolley et al. 2014; Rus and Tolley 2015). This deformation can enter geometrically nonlinear regime and is often coupled with the mechanics of the surrounding medium, leading to a challenging fluid-structure interaction problem.

Nature offers a rich set of solutions to engineers seeking to design robots with locomotive ability. Depending on the mechanics of the medium, locomotion can face unique physical constraints, e.g. at fluid flow with low Reynolds number (viscous forces dominate inertia), scallop theorem states that a swimmer with time reversible motion cannot achieve propulsion (Lauga 2011). Over the past two decades, a large number of studies have been conducted on the locomotion of aquatic animals and bioinspired robots living in aquatic environment across a broad range of Reynolds number, e.g. flagellates (Scaramuzza et al. 2009; Thawani and Tirumkudulu 2018; Forghani et al. 2021), turtles (Licht et al. 2004), eels (Yu et al. 2012), fish (Saimek and Li 2004;

Conte et al. 2010; Bartlett et al. 2017), and octopus (Laschi et al. 2012; Renda et al. 2018).

Compared with underwater locomotion, the mechanisms for underground locomotion are far less understood. This is partly due to the outstanding challenges in modeling the mechanics of granular medium and coupling it with deformable solids. Nonetheless, desert animals, such as scorpions, snakes, and lizards, show remarkable capabilities in dissipating heat from their body, facilitating feeding, reproducing, and escaping from predators. These slender flexible animals have evolved to apply a variety of locomotion modes depending on their physiology and environmental factors; most common of them are walking, running, jumping, swimming and flying (Gray 1968; Biewener 1990; Dickinson et al. 2000; Alexander 2003; Taylor et al. 2003). A comprehensive understanding of locomotion of soft bodies in granular medium can lead to novel design of bio-inspired robots for application in hazardous terrain, e.g. search and reconnaissance through debris and underground environmental monitoring.

¹Department of Mechanical & Aerospace Engineering, University of California Los Angeles, Los Angeles, California 90095 USA

Corresponding author:

M. Khalid Jawed, Department of Mechanical & Aerospace Engineering, University of California Los Angeles, Los Angeles, California 90095, USA
Email: khalidjm@seas.ucla.edu

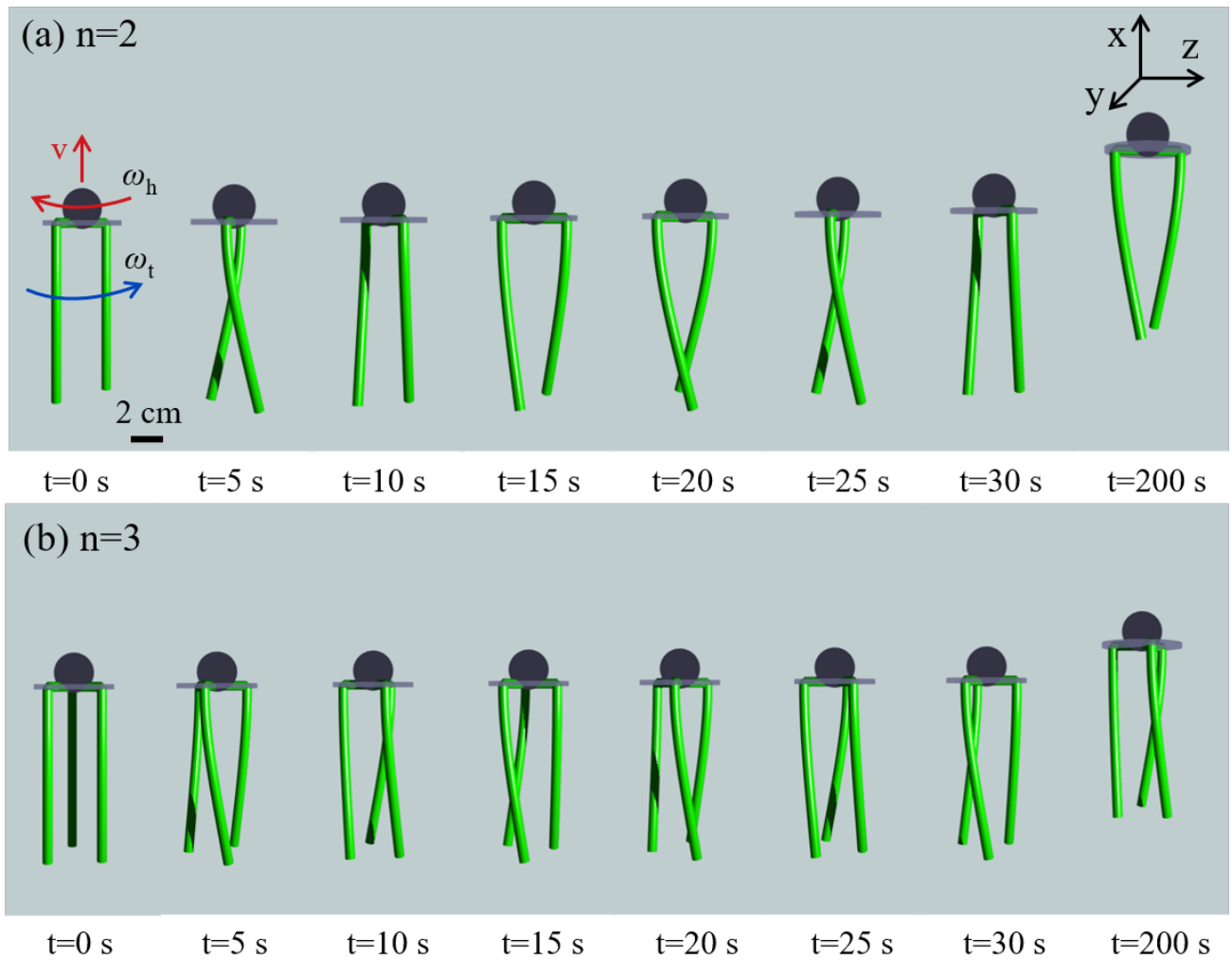


Figure 1. Snapshots from simulation. The shape of a robot with (a) $n = 2$ tails (Rotational speed of the motor $\omega_T = 100.00$ rpm, head rotational speed $\omega_h = 95.47$ rpm, tail rotational speed $\omega_t = 4.53$ rpm) and (b) $n = 3$ tails ($\omega_T = 100.00$ rpm, $\omega_h = 97.49$ rpm, $\omega_t = 2.51$ rpm) between $t = 0$ and $t = 200$ seconds. The speed of the robot is $v = 0.22$ mm/s (and $v = 0.13$ mm/s) for $n = 2$ (and $n = 3$).

Fortunately, it has recently been shown that granular flow can be functionally equivalent to low Reynolds fluid flow (Zhang and Goldman 2014). Flagellar propulsion, widely studied since 1955 (Gray and Hancock 1955) for application in low Reynolds fluid medium, is effective in granular medium as well (Texier et al. 2017). This builds a remarkable connection between the microscopic world of bacteria (Lauga and Powers 2009) and meter-sized snakes in sand. The benefits of the flexibility of flagella, e.g. tumbling (Macnab and Ornston 1977) and turning (Son et al. 2013) during swimming, in viscous fluid can potentially be employed in robots for underground locomotion.

In this paper, we draw inspiration from propulsion of bacteria and introduce a palm-sized untethered robot comprised of $n \geq 2$ naturally straight elastic rods and a rigid head with embedded motor and battery. As shown in Figure 1, the rotation of these *tails* brings about drag loading from the granular medium causing deformation in the soft material. As a result, the tails assume a nonlinear shape that provides a net propulsive force forward. This net propulsion is only feasible in flexible structures; in case of *rigid* straight tails, the propulsion is zero. We introduce a numerical

method for simulation of the dynamics of a collection of Kirchhoff elastic rods (Kirchhoff 1859) under viscous drag described by Resistive Force Theory (RFT) (Gray and Hancock 1955). This computational tool is used to simulate the multi-limbed robot and quantitatively compared against experiments. We perform parametric studies on the speed of the robot as a function of the number of tails and rotational speed, and evaluate the optimal rotational speed for maximum efficiency. We test the applicability of RFT to granular medium and indicate regimes where this theory can fail.

2 Background and related work

The problem at hand can be divided into two components: (1) the modeling of the external loading on the flexible structure of the surrounding medium and (2) the mechanics of slender bodies composed of multiple thin elastic rods.

2.1 Model of external loading in granular medium

A major challenge of modeling the nonlinear dynamics of soft robot swimming in granular media is to understand the external forces on thin filaments within sand, soil, muddy sediments and otherwise mechanically unstable terrestrial substrates that display both solid and fluid-like behavior. Desert sand is an example of these kinds of granular materials that can display solid-like behavior in bulk and fluid-like features when disturbed. In case of purely fluid medium, modeling the motion of soft robot is always possible in principle because the rules of interaction with fluids can be worked out by solving Navier-Stokes hydrodynamics in the presence of moving boundary conditions. However, the computational cost is prohibitive for application in design and control of soft robots. For rods – mechanical structures with one dimension much larger than the other two – moving in low Reynolds flow, RFT is widely used to connect the hydrodynamic force from viscous environment and the velocity along the rod’s centerline (Gray and Hancock 1955; Lighthill 1976; Johnson and Brokaw 1979; Rodenborn et al. 2013). Despite differences in the physical mechanisms involved, a solid friction analog to RFT in viscous fluid has been successfully applied in the context of granular media to describe the undulatory motion of sand lizards and snakes (Hu et al. 2009; Maladen et al. 2011b). It has also been reported that, during the movement in granular media, the primary propulsive force in slithering is generated by the anisotropic friction force of the rod surface against the substrate (Hu et al. 2009) – a mechanism reminiscent of the propulsion of bacterial flagella in viscous fluid medium. Since then, several studies have shown that the frictional forces occurring perpendicular to the body per unit length are greater than those along the body (Maladen et al. 2009; Ding et al. 2012; Texier et al. 2017).

2.2 Mechanics of branched elastic rod structures

The external force from granular medium can result in geometrically nonlinear deformation in the elastic rods, as shown in Figure 1. This coupling between the structural deformation and the forces from the granular medium in the context of an articulated soft robot is yet to be addressed in the literature. Notable prior works investigated the force on thin *rigid* rods in viscous fluid (Lighthill 1976; Rodenborn et al. 2013; Thawani and Tirumkudulu 2018) or granular medium (Texier et al. 2017; Thawani and Tirumkudulu 2018). In our study, we use the Discrete Elastic Rods (DER) algorithm (Bergou et al. 2008, 2010; Jawed et al. 2018) to capture the nonlinear deformation of thin elastic rods in the presence of external forces. DER method was first introduced in the computer graphics community for fast simulation of the visually dramatic dynamics of hair and other filamentary structures. Previous studies combined DER method with hydrodynamic models for viscous fluid to investigate the deformation and instability of helical elastic rod – an analog for bacterial flagellum (Jawed et al. 2015; Jawed and Reis 2016, 2017). All of these studies considered only a single elastic rod that is deforming due to hydrodynamic forces.

More recently, we studied a model uniflagellar bacteria (a helical elastic rod attached to a rigid spherical head) and considered the interaction between the flows induced by the rod and the head (Forghani et al. 2021).

A wide variety of soft robots can be modeled as a network of multiple elastic rods, optionally connected to rigid bodies. Structures comprised of multiple elastic rods, e.g. elastic gridshell (also known as Cosserat net) (Baek et al. 2018) and flexible rod mesh Pérez et al. (2015), have also been modeled using DER. The multi-rod gridshell simulator (Baek et al. 2018) used stiff springs at the joints between two rods to impose constraints and treated the spring forces explicitly. This requires small time step size, compared with a fully implicit approach, for numerical simulation and ignores the coupling of twisting and bending modes (Pérez et al. 2015) between two rods at the joints. In this study, we present a simulation algorithm that treats all the elastic and external forces implicitly in a network of rods and accounts for the presence of a rigid head. We demonstrate that a seemingly complex robot can be kinematically represented by a network of rods; this rod-based presentation can be used to leverage the computational efficiency of cutting edge tools like DER.

This paper is organized as follows. Section *Experimental design* provides a detailed description of the robotic platform and the experimental setup. Next the numerical model we employ for simulating the locomotion of multi-limbed robot is introduced in Section *Numerical model description*. The results from simulations and experiments are presented in Section *Results and discussion*. Finally conclusions obtained are summarized and future research directions are suggested in Section *Conclusion*.

3 Experimental design

The primary purpose of our experiments is to investigate the motion of a robot propelled by multiple elastic rods undergoing rotation. We place emphasis on the conditions and restrictions pertinent to RFT’s application to model the drag from granular media. Keeping this goal in mind, we sequentially describe the design of the robot, fabrication, experimental setup, and data analysis in the following.

3.1 Robotic platform design

Figure 2(a) shows a photograph of the soft robot which is a small, lightweight (14 cm, 35 g) structure actuated by n number of soft elastic tails. It includes (1) a head with two 3.7V 200mAh rechargeable 502025 LiPo batteries and one DC geared motor (uxcell) with 3V nominal voltage, 0.35W nominal power and 0.55A stall current, (2) multiple elastic tails, and (3) one 3D-printed plate to hold those tails. Inside the head, two batteries are connected in parallel, naturally making the entire structure symmetric. Inspired by the head shape of desert animals such as scorpions, snakes and lizards not being perfectly spherical, we design the shape of our robot head to be cuboid to increase the ability to fluidize the granular medium in front of it. Our idea is empirically verified by the much slower movement and higher slippage occurrence of the robot with a spherical head compared to that with a cuboid head. We vary the number of robot tails to explore its effect on the translational speed, v , of our

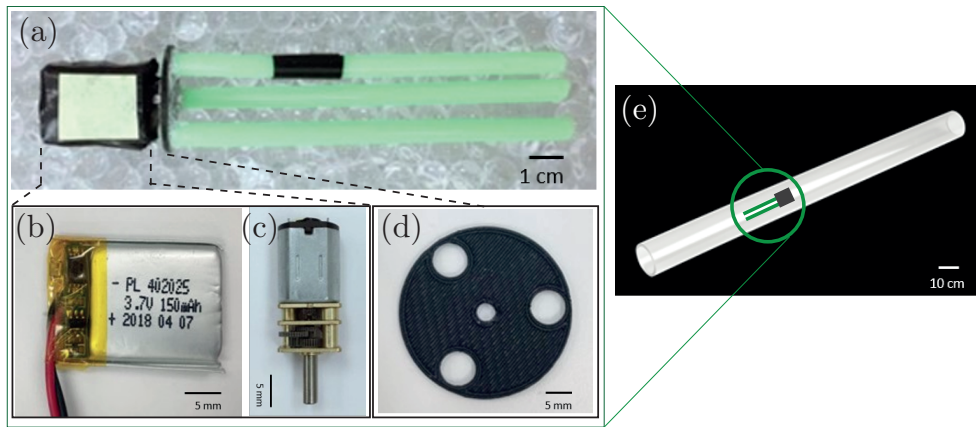


Figure 2. The composite view of the experimental setup. (a) The robot with $n = 3$ tails. The head is comprised of (b) a battery and (c) a motor. (d) A circular disc connects the tails with the head. (e) The robot is placed inside a cylindrical tube full of granular medium.

robot. All tails are glued to the 3D-printed plate and they are driven by a single motor through the motor shaft, protruding from the head of the robot. The control parameter is the rotational speed of the tails relative to the head, ω_T . To vary this parameter, we fabricate robots with different gear motors while keeping all other components the same. The rotational speed of the gear motor is related to the voltage provided, and it will decrease when the voltage is lower. To keep the motor rotation speed consistent, we fully charge the batteries for each experimental trial and recharge the battery after every experiment that lasts for approximately 10 minutes. During data analysis, we count the number of rotations with time and find that this protocol has ensured a constant rotational speed during the entire experimental trial. Moreover, the size and weight of all the motors are almost the same, $13 - 15\text{g}$ and $(15 - 17) \times 12 \times 10\text{mm}$ even though they provide different rotational speeds. When necessary, we add electrical tapes around the motor to account for the small differences in size and weight among different motors.

3.2 Granular medium

We choose water crystal bead as the granular medium to test the locomotion due to its transparency. The robot can be seen from outside the medium using a conventional digital camera (Nikon D3400). The diameter of the beads in dry state is 2.5 mm , which increases to $d_b = 9.4 \pm 0.4\text{ mm}$ after fully absorbing water. The size of beads is controllable by controlling the time they are placed inside water and changeable reversibly after dehydration. Due to this property, the water crystal beads can also be used to investigate the performance of the robot, efficiency to be mentioned in section 6 for example, related to the granule configuration, such as size, density and homogeneity. When performing experiments, we use the beads fully absorbing water to ensure that the size is consistent. Before experiments are carried out, we dry their surfaces so as to decrease the occurrence possibility of slippage between the granular medium and the robot. The volume fraction – the ratio between the solid volume and the occupied volume – is approximately 0.52 . The volume fraction is stated to control the response of granular media to intrusion (Maladen et al. 2009) and we will discuss how it might be related to the

“stick slip” in Section 5. It is noticeable from Figure 2(a) that the diameter of the bead is on the same order of magnitude as the diameter of the tails. RFT is intended for grains that are much smaller than the size of the robot; our choice of rather large grains is to test the limits of applicability of RFT.

3.3 Fabrication of elastic tails

The elastic tails were fabricated using a molding and casting technique developed by Lazarus et al. (2013) and Miller et al. (2014). A 50% - 50% mixture by mass of catalyst and base of a silicone-based rubber (Vinylpolysiloxane, Elite Zhermack) was injected into a PVC tube (VWR International) of inner and outer diameters are 3.175 mm and 6.35 mm , respectively. The PVC tube mold were affixed to a straight steel bar to hold the shape completely straight. The mixture was allowed to cure undisturbed for 24 hours. The PVC tube was then carefully cut to extract the now solid VPS rod. The radius of elastic tails can be changed by using PVC tubes with different inner and outer diameters, making the scale-up or scale-down of our robot platform effortless.

3.4 Locomotion experiments

As the reservoir of granular medium, we use a cylindrical transparent tube with with an inner radius of 53 mm and axial length of 1220 mm . The tube is filled with granular medium and placed horizontally (perpendicular to the direction of gravity). The robot is initially placed at one end near the center of the cross-section of the tube, meant to cancel the wall effect. Since the robot is placed at the center of the tube, surrounded by compact granules against the tube wall, the drag-induced lift mentioned in Maladen et al. (2011a) is suppressed. Hence, the rotation of tails will move the robot forward through the granular medium along an approximately straight line. Movements of the robot are captured by a video camera at a frame rate of 29.98 fps . In order to count the rotational speed of the robot head (ω_h) and tail (ω_t), a bright yellow marker is attached to the black colored head and a black marker is put onto one of the green colored elastic tails.

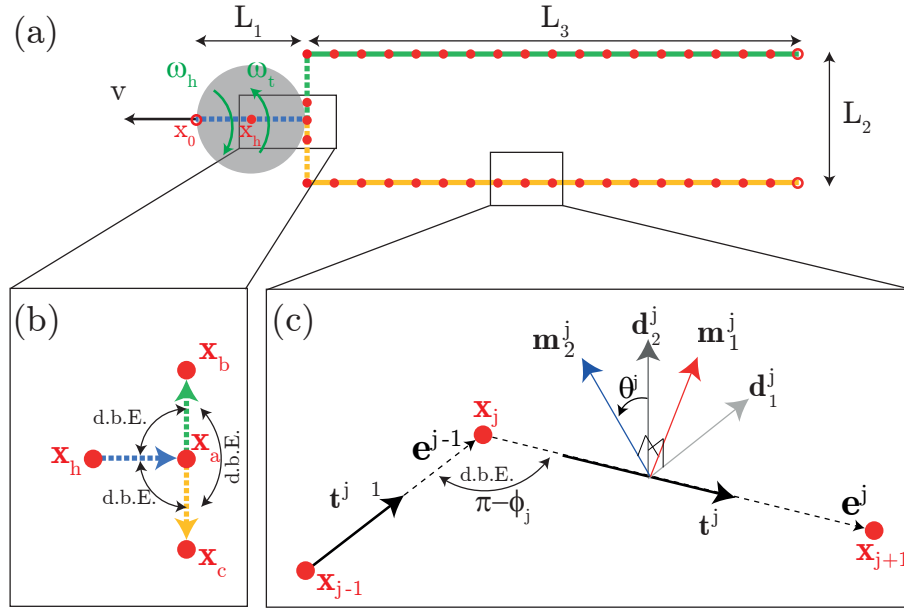


Figure 3. Schematic of the discrete representation of a robot with two tails. (a) Geometric parameters of the robot in undeformed state. Here, $L_1 = 2a$ is the diameter of the robot head, L_2 is the diameter of the disc connecting the head and the tails, and L_3 is the length of each tail. Dashed lines represent rigid structure whereas solid lines correspond to flexible structure. The node \mathbf{x}_h represents the location of the head. (b) A close-up view of the “joint” node \mathbf{x}_a that connects the head with the tails. In this figure, d.b.E. indicates discrete bending and twisting energy. This is the only node that is connected to more than two nodes. (c) A close-up view of three nodes, \mathbf{x}_{j-1} , \mathbf{x}_j , and \mathbf{x}_{j+1} , and two edges, $\mathbf{e}^{j-1} = \mathbf{x}_j - \mathbf{x}_{j-1}$ and $\mathbf{e}^j = \mathbf{x}_{j+1} - \mathbf{x}_j$. The turning angle, ϕ_j , between the two edges result in bending energy and the rotation of the material frame from one edge to the next result in twisting energy. The reference frame on \mathbf{e}^j is $\{\mathbf{d}_1^j, \mathbf{d}_2^j, \mathbf{t}^j\}$ and the material frame is $\{\mathbf{m}_1^j, \mathbf{m}_2^j, \mathbf{t}^j\}$. The twist angle on that edge is θ^j .

4 Numerical model description

This section introduces a numerical model of the robot where the robotic structure is represented using a network of Kirchhoff’s rods Kirchhoff (1859). This model is used in a numerical simulation scheme that solves the equations of motion at each degree of freedom (DOF). The simulation is subsequently utilized to extract various locomotion parameters, e.g. speed of the robot and its efficiency.

4.1 Kinematics

Referring to Figure 3(a), the first step in the modelling process is representing the robot as a “stick figure”. A number of nodes (circles in Figure 3) are located along the stick figure. Figure 3(b) shows the nodes at the junction between the head and the tails ($n = 2$ in the figure). Node \mathbf{x}_a is unique since it is connected to $n + 1$ nodes. All the other nodes are connected to two nodes or, in case of terminal nodes (open circles in Figure 3(a)), one node. As shown in Figure 3(c), typically a node \mathbf{x}_j is connected with two nodes \mathbf{x}_{j-1} and \mathbf{x}_{j+1} . The vector connecting two consecutive nodes (e.g. $\mathbf{e}^j = \mathbf{x}_{j+1} - \mathbf{x}_j$) is called an “edge”. In addition to the location of the nodes, a complete description of the robotic structure requires a measure of the rotation of the edges. A material frame $\{\mathbf{m}_1^j, \mathbf{m}_2^j, \mathbf{t}^j\}$ (j represents the edge number) is associated with each edge to keep track of rotation. This frame is orthonormal and adapted, i.e. the third director $\mathbf{t}^j = \mathbf{e}^j / \|\mathbf{e}^j\|$ is the tangent along the edge ($\|\cdot\|$ represents the Euclidean norm of a vector). Another orthonormal adapted frame $\{\mathbf{d}_1^j, \mathbf{d}_2^j, \mathbf{t}^j\}$ is used as the reference frame. This frame is initialized at time

$t = 0$ and then updated at every time step of the simulation through time-parallel transport; details will be provided later in this paper. A single scalar quantity, θ^j , is necessary per edge to obtain the material frame from the reference frame as outlined in the following two equations:

$$\mathbf{m}_1^j = \mathbf{d}_1^j \cos \theta^j + \mathbf{d}_2^j \sin \theta^j \quad (1a)$$

$$\mathbf{m}_2^j = -\mathbf{d}_1^j \sin \theta^j + \mathbf{d}_2^j \cos \theta^j \quad (1b)$$

The angle θ^j is referred to as the “twist angle”. We follow the convention of using subscripts to denote node-based quantities and superscripts for edge-based quantities.

The locations of the nodes, \mathbf{x}_j ($0 \leq j < N$ where N is the number of nodes), and the twist angles, θ^j ($0 \leq j < N_e$ where N_e is the number of edges), completely describe the configuration of the robot. For the robot studied in this paper, it turns out that $N_e = N - 1$ (see Figure 3(a)). The DOF vector for the robot is

$$\mathbf{q} = [\mathbf{x}_0, \mathbf{x}_1, \mathbf{x}_2, \dots, \mathbf{x}_{N-1}, \theta^0, \theta^1, \dots, \theta^{N_e-1}]^T, \quad (2)$$

where the superscript T denotes transpose. If a robot has N nodes, the size of \mathbf{q} is $\text{ndof} = 3 \times N + N_e$. Since the robot deforms with time, the DOF vector is a function of time, i.e. $\mathbf{q} \equiv \mathbf{q}(t)$. Knowing the configuration of the robot at $t = 0$ (i.e. $\mathbf{q}(0)$ is known), the task at hand is to compute $\mathbf{q}(t)$. This is achieved by discretizing the time into small steps of step size Δt and solving the equations of motion at each time step.

Equations of motion are statements of balance of forces. The internal forces in the robotic structure arises from the elastic nature of the material. In this paper, the rigid components of the robot (e.g. the head and the disc indicated

by dashed lines in Figure 3(a)) are assumed to be elastic with high elastic stiffness so that the deformation in these components are negligible compared with the deformation in the flexible tails. In the following, the strains in the structure, the elastic energies associated with these strains, and the elastic and external forces are sequentially discussed.

4.2 Macroscopic strains

At time $t = 0$, the robot is undeformed with zero strains and DOF vector is $\mathbf{q}(0) \equiv \bar{\mathbf{q}}$; hereafter, $(\bar{\cdot})$ represents evaluation of a quantity in undeformed configuration. Even though the undeformed and initial configurations are the same in the system studied here, this is not a required assumption for the simulation scheme.

Axial stretch, curvature, and twist are the macroscopic strains along the structure Audoly and Pomeau (2000). As outlined next, these strain measures can be computed from the DOF vector \mathbf{q} and are used to compute the elastic energy.

Axial stretch is an edge-based quantity that is related to the elongation of an edge. The axial stretch, ϵ^j , in the j -th edge is

$$\epsilon^j = \frac{\|\mathbf{e}^j\|}{\|\bar{\mathbf{e}}^j\|} - 1. \quad (3)$$

Curvature is a node-based quantity that is related to the turning angle ϕ_j (see Figure 3(c)). No curvature is associated with the terminal nodes. Curvature binormal is a vector representing the turn:

$$(\kappa\mathbf{b})_j = \frac{2\mathbf{e}^{j-1} \times \mathbf{e}^j}{\|\mathbf{e}^{j-1}\| \|\mathbf{e}^j\| + \mathbf{e}^{j-1} \cdot \mathbf{e}^j}. \quad (4)$$

It turns out that $\|(\kappa\mathbf{b})_j\| = 2 \tan\left(\frac{\phi_j}{2}\right)$. The curvature of the osculating circle passing through \mathbf{x}_{j-1} , \mathbf{x}_j , and \mathbf{x}_{j+1} is $\|(\kappa\mathbf{b})_j\|/\Delta l$ where $\Delta l = \|\mathbf{e}^j\| = \|\mathbf{e}^{j-1}\|$. The scalar curvatures along the first and second material directors are

$$\kappa_j^{(1)} = \frac{1}{2}(\mathbf{m}_2^{j-1} + \mathbf{m}_2^j) \cdot (\kappa\mathbf{b})_j, \quad (5a)$$

$$\kappa_j^{(2)} = \frac{1}{2}(\mathbf{m}_1^{j-1} + \mathbf{m}_1^j) \cdot (\kappa\mathbf{b})_j. \quad (5b)$$

Associated with every curvature is a twist that represents the rotation of the material frame from one edge to the next edge. In Figure 3(c), the twist at the j -th node is

$$\tau_j = \theta^j - \theta^{j-1} + \Delta m_{j,\text{ref}}, \quad (6)$$

where $\Delta m_{j,\text{ref}}$ is the reference twist that represents the twist of the reference frame as it moves from the $(j-1)$ -th edge to the j -th edge. The procedure to calculating this reference twist is discussed next. The first director of the reference frame, \mathbf{d}_1^{j-1} , is *parallel transported* from the $(j-1)$ -th edge to the j -th edge to get \mathbf{d}_{imp} . Parallel transport is the process of moving the reference director from one edge to the next without twist; it involves the following steps.

$$\begin{aligned} \mathbf{b} &= \mathbf{t}^{j-1} \times \mathbf{t}^j, \\ \hat{\mathbf{b}} &= \frac{\mathbf{b}}{|\mathbf{b}|}, \\ \mathbf{n}_1 &= \mathbf{t}^{j-1} \times \hat{\mathbf{b}}, \\ \mathbf{n}_2 &= \mathbf{t}^j \times \hat{\mathbf{b}}, \\ \mathbf{d}_{\text{imp}} &= (\mathbf{d}_1^{j-1} \cdot \mathbf{t}^{j-1})\mathbf{t}^j + (\mathbf{d}_1^{j-1} \cdot \mathbf{n}_1)\mathbf{n}_2 + (\mathbf{d}_1^{j-1} \cdot \hat{\mathbf{b}})\hat{\mathbf{b}}, \end{aligned}$$

where \mathbf{t}^{j-1} and \mathbf{t}^j are the tangents on the $(j-1)$ -th and j -th edges, respectively. The reference twist, $\Delta m_{j,\text{ref}}$, is the signed angle from \mathbf{d}_{imp} to \mathbf{d}_1^j about \mathbf{t}^j .

4.3 Elastic energies

The total elastic energy of the structure is the linear sum of stretching, bending, and twisting energies such that

$$E_{\text{elastic}} = E_s + E_b + E_t, \quad (7)$$

where E_s , E_b , and E_t are the stretching, bending, and twisting energies, respectively.

Associated with each edge is a discrete stretching energy that can be computed from the axial stretch in Eq. 3,

$$E_s = \sum \frac{1}{2} EA (\epsilon^j)^2 \|\bar{\mathbf{e}}^j\|, \quad (8)$$

where \sum represents summation over all the edges, E is the Young's modulus, $A = \pi r_0^2$ is the cross-sectional area, r_0 is the cross-sectional radius. For the edges that are located on rigid part of the robot (head and disc), the parameter EA is taken to be sufficiently large so that the deformation is negligible.

The bending energy is

$$E_b = \sum \frac{1}{2} \frac{EI}{\Delta l_j} \left[\left(\kappa_j^{(1)} - \bar{\kappa}_j^{(1)} \right)^2 + \left(\kappa_j^{(2)} - \bar{\kappa}_j^{(2)} \right)^2 \right], \quad (9)$$

where \sum represents summation over all the curvatures, $\Delta l_j = \frac{1}{2} (\|\bar{\mathbf{e}}^{j-1}\| + \|\bar{\mathbf{e}}^j\|)$ is the Voronoi length associated with the j -th node, $\bar{\kappa}_j^{(1)}$ and $\bar{\kappa}_j^{(2)}$ are the material curvatures in undeformed configuration, and $EI = \frac{\pi}{4} E r_0^4$ is the bending stiffness. To model rigid components of the robot, the bending stiffness is assumed to be large enough so that the curvatures at the rigid nodes remain almost constant throughout the simulation.

The twisting energy is

$$E_t = \sum \frac{1}{2} \frac{GJ}{\Delta l_j} (\tau_j - \bar{\tau}_j)^2, \quad (10)$$

where $\bar{\tau}_j$ is the undeformed twist along the centerline, G is the shear modulus, and $GJ = \frac{\pi}{2} G r_0^2$ is the twisting stiffness. This stiffness is assumed to be sufficiently large for the rigid components. The material of the tail is nearly incompressible (i.e. Poisson's ratio $\nu = 0.5$) and therefore $G = E/3$.

In case of a single elastic rod, each internal node is associated with a discrete bending energy and a discrete twisting energy. However, the robot is represented as a network of rods and the "joint" node (\mathbf{x}_a in Figure 3(b)) has multiple discrete bending energies (indicated by d.B.E. in Figure 3(b)) and discrete twisting energies associated with it. This observation is important during the programming implementation of the simulation algorithm.

4.4 External forces using Resistive Force Theory

First, the external force on the tails exerted by the granular medium following RFT is discussed. In Figure 4, we schematically represent a slender rod in discrete setting moving in the granular medium. The velocity, $\mathbf{v}_j \equiv \dot{\mathbf{x}}_j$ at

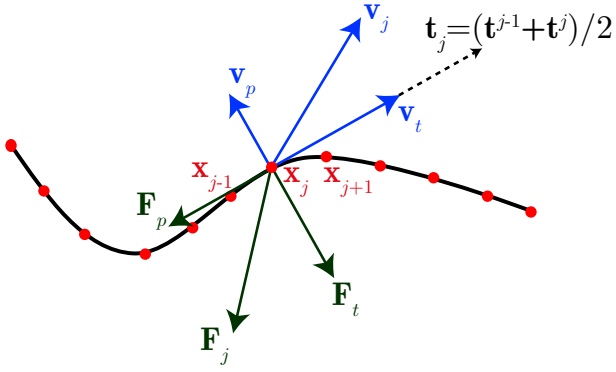


Figure 4. Schematic representation of RFT.

point \mathbf{x}_j can be decomposed into two parts: the parallel term $\mathbf{v}_t = (\mathbf{v}_j \cdot \mathbf{t}_j)\mathbf{t}_j$ and the perpendicular term $\mathbf{v}_p = \mathbf{v}_j - \mathbf{v}_t$, where the tangent at the j -th node $\mathbf{t}_j = \frac{1}{2}(\mathbf{t}^{j-1} + \mathbf{t}^j)$ is the average of the tangents along the two associated edges. The tangential and perpendicular forces from the medium that resist \mathbf{v}_t and \mathbf{v}_p are

$$\mathbf{F}_t = -\eta_t \mathbf{v}_t \Delta l_j, \quad (11a)$$

$$\mathbf{F}_p = -\eta_p \mathbf{v}_p \Delta l_j, \quad (11b)$$

where the drag coefficients along the tangential and perpendicular directions (Gray and Hancock 1955) are

$$\eta_t = 2\pi\mu / \left[\log\left(\frac{2L}{r_0}\right) - \frac{1}{2} \right] \quad (12a)$$

$$\eta_p = 4\pi\mu / \left[\log\left(\frac{2L}{r_0}\right) + \frac{1}{2} \right], \quad (12b)$$

μ is the dynamic viscosity, and L is the length of tail ($L = L_3$ in Figure 3(a)). The external force on the j -th node, if this node is located on the tails, is

$$\mathbf{F}_j = \mathbf{F}_t + \mathbf{F}_p. \quad (13)$$

In addition to the tails, the head of the robot is also rotating and translating. The rotational speed of the head (ω_h in Figure 3) can be extracted from the time derivative of the twist angle, θ^h , of the edge connected \mathbf{x}_0 and \mathbf{x}_h , i.e. $\omega_h \equiv \dot{\theta}^h$. The velocity of the head, \mathbf{v}_h is the time derivative of \mathbf{x}_h , i.e. $\mathbf{v}_h \equiv \dot{\mathbf{x}}_h$. If the head was spherical with radius a , the viscous drag according to Stokes's law would result in an external force on \mathbf{x}_h ,

$$\mathbf{F}_h = -6\pi\mu a \mathbf{v}_h, \quad (14)$$

and an external torque on the edge (with twist angle θ^h),

$$T_h = -8\pi\mu a^3 \omega_h. \quad (15)$$

In our case, the robot head shape is not a sphere and we cannot directly apply Eqs. 14 and 15. Instead, we use a numerical coefficient, C_1 , to account for the shape of the robot head. As a result, Eq. 14 is updated as follows

$$\mathbf{F}_h = -(6\pi C_1)\mu a \mathbf{v}_h. \quad (16)$$

Similarly, Eq. 15 is updated to include a numerical coefficient, C_2 , that accounts for the nonspherical shape of the head:

$$T_h = -(8\pi C_2)\mu a^3 \omega_h. \quad (17)$$

The coefficients C_1 and C_2 are used as fitting parameters in Section 5.3 and obtained through data fitting.

4.5 Simulation loop, equations of motion

In the simulation scheme (Algorithm 1), time is discretized into small time-steps and the configuration of the robot represented by the DOF vector, \mathbf{q} , is updated at each time step. The equation of motion at the i -th DOF to march from $t = t_k$ to $t = t_{k+1} = t_k + \Delta t$ (Δt is the time step size) is

$$f_i \equiv \frac{m_i}{\Delta t} \left[\frac{q_i(t_{k+1}) - q_i(t_k)}{\Delta t} - \dot{q}_i(t_k) \right] + \frac{\partial E_{\text{elastic}}}{\partial q_i} - f_i^{\text{ext}} = 0, \quad (18)$$

where $i = 1, \dots, \text{ndof}$, the *old* DOF $q_i(t_k)$ and velocity $\dot{q}_i(t_k)$ are known, E_{elastic} is the elastic energy evaluated at $q_i(t_{k+1})$, f_i^{ext} is the external force (or moment for twist angles) on the i -th DOF, and m_i is the lumped mass at each DOF. Since the dynamics of the system is dominated by viscosity with negligible influence of inertia, the results presented in this paper do not vary with the mass parameters as long as low Reynolds number is maintained. Note that Eq. 18 is simply a statement of “mass times acceleration = elastic force + external force” at the i -th DOF. Eq. 18 represents a system of ndof equations that has to be solved to obtain the *new* DOF $q_i(t_{k+1})$. Once the new DOF is obtain, the new velocity is simply $\dot{q}_i(t_{k+1}) = (q_i(t_{k+1}) - q_i(t_k)) / \Delta t$.

Newton-Raphson method is used to solve the equations of motion. Referring to Algorithm 1, this involves solving the following linear system of size ndof ,

$$\mathbb{J} \Delta \mathbf{q} = \mathbf{f}, \quad (19)$$

where \mathbf{f} is a vector of size ndof , the i -th component of this vector can be computed from Eq. 18, and \mathbb{J} is a square matrix representing the Jacobian for Eq. 18. The (i, j) -th component of the Jacobian is

$$\mathbb{J}_{ij} = \frac{\partial f_i}{\partial \xi_j} = \mathbb{J}_{ij}^{\text{inertia}} + \mathbb{J}_{ij}^{\text{elastic}} + \mathbb{J}_{ij}^{\text{ext}}, \quad (20)$$

where

$$\mathbb{J}_{ij}^{\text{inertia}} = \frac{m_i}{\Delta t^2} \delta_{ij}, \quad (21)$$

$$\mathbb{J}_{ij}^{\text{elastic}} = \frac{\partial^2 E_{\text{elastic}}}{\partial q_i \partial q_j}, \quad (22)$$

$$\mathbb{J}_{ij}^{\text{ext}} = -\frac{\partial f_i^{\text{ext}}}{\partial q_j}. \quad (23)$$

Here, δ_{ij} represents Kronecker delta. Evaluation of the gradient of the elastic energy ($\frac{\partial E_{\text{elastic}}}{\partial q_i}$) as well as its Hessian ($\frac{\partial^2 E_{\text{elastic}}}{\partial q_i \partial q_j}$) are well documented in Jawed et al. (2018); Bergou et al. (2010).

4.6 Actuation of the robot

An important contribution of this study is the observation that the actuation (e.g. rotation of motor in the robot) can be readily accounted for in the above framework by updating the undeformed configurations with time. Typically, undeformed configuration of a structure is fixed and assumed to be constant through the simulation. The strains in undeformed configuration (e.g. $\bar{\kappa}_j^{(1)}, \bar{\kappa}_j^{(2)}, \bar{\tau}_j$) are used in calculation of elastic energies, their gradient (i.e. elastic forces), and

Algorithm 1 Discrete Simulation of Robots

Require: $\mathbf{q}(t_k), \dot{\mathbf{q}}(t_k)$ // DOFs and velocities at $t = t_j$
Require: $(\mathbf{d}_1^j(t_k), \mathbf{d}_2^j(t_k), \mathbf{t}^j(t_k)), 0 \leq j < N_e$ // Reference frame at $t = t_k$
Ensure: $\mathbf{q}(t_{k+1}), \dot{\mathbf{q}}(t_{k+1})$ // DOFs and velocities at $t = t_{k+1}$
Ensure: $(\mathbf{d}_1^j(t_{k+1}), \mathbf{d}_2^j(t_{k+1}), \mathbf{t}^j(t_{k+1})), 0 \leq j < N_e$ // Reference frame at $t = t_{k+1}$

1: **function** DISCRETE SIMULATION OF ROBOTS($\mathbf{q}(t_k), \dot{\mathbf{q}}(t_k), (\mathbf{a}_1^j(t_k), \mathbf{a}_2^j(t_k), \mathbf{t}^j(t_k))$)
2: $\bar{\tau}_h(t_k) \leftarrow \omega_T t_k$ // Actuation using Eq. 24
3: **Guess:** $\mathbf{q}^{(1)} \leftarrow \mathbf{q}(t_k)$
4: $n \leftarrow 1$
5: **while** error > tolerance **do** // Newton-Raphson iterations
6: Compute reference frame $(\mathbf{d}_1^j, \mathbf{d}_2^j, \mathbf{t}^j)^{(n)}$ // Parallel transport $\mathbf{d}_1^j(t_k)$ and $\mathbf{d}_2^j(t_k)$ from ...
7: // ... $\mathbf{t}^j(t_k)$ to tangent on j -th edge in $\mathbf{q}^{(n)}$ to get $(\mathbf{d}_1^j)^{(n)}$ and $(\mathbf{d}_2^j)^{(n)}$
8: Compute reference twist $\Delta m_{j,\text{ref}}^{(n)}$ at each internal node
9: Compute material frame $(\mathbf{m}_1^j, \mathbf{m}_2^j, \mathbf{t}^j)^{(n)}$ // Eq. 1
10: Compute \mathbf{f} and \mathbb{J} // Eqs. 18 and 20
11: $\Delta \mathbf{q} \leftarrow \mathbb{J} \backslash \mathbf{f}$
12: $\mathbf{q}^{(n+1)} \leftarrow \mathbf{q}^{(n)} - \Delta \mathbf{q}$ // Update DOFs
13: error $\leftarrow \text{sum}(\text{abs}(\mathbf{f}))$
14: $n \leftarrow n + 1$
15: **end while**

16: $\mathbf{q}(t_{k+1}) \leftarrow \mathbf{q}^{(n)}$
17: $\dot{\mathbf{q}}(t_{k+1}) \leftarrow \frac{\mathbf{q}(t_{k+1}) - \mathbf{q}(t_k)}{\Delta t}$
18: $(\mathbf{d}_1^j(t_{k+1}), \mathbf{d}_2^j(t_{k+1}), \mathbf{t}^j(t_{k+1})) \leftarrow (\mathbf{d}_1^j, \mathbf{d}_2^j, \mathbf{t}^j)^{(n)}$
19: **return** $\mathbf{q}(t_{k+1}), \dot{\mathbf{q}}(t_{k+1}), (\mathbf{d}_1^j(t_{k+1}), \mathbf{d}_2^j(t_{k+1}), \mathbf{t}^j(t_{k+1}))$
20: **end function**

Hessian. However, in case of this robot, the rotation of the motor causes the undeformed twist at the head node (\mathbf{x}_h) to vary with time. If the rotational speed of the motor is ω_T , we assume that the undeformed twist at the head node is

$$\bar{\tau}_h(t_k) = \omega_T t_k. \quad (24)$$

This results in rotations of the head (ω_h) and the tails (ω_t) along opposite directions such that $|\omega_T| = |\omega_h| + |\omega_t|$. The total rotational speed, ω_T , is a control parameter in this study.

4.7 Remarks on implementation of the algorithm

The most computationally expensive part of Algorithm 1 is solving the linear system (Line 11). To reduce computation time, it is important to observe the sparsity of the Jacobian matrix, \mathbb{J} , and exploit this sparsity during the solution process (Schenk and Gärtner 2002). Referring to Figure 3(c), the entire structure can be assumed to be a combination of stretching springs (e.g. one stretching spring is between \mathbf{x}_j and \mathbf{x}_{j+1}) and bending-twisting springs (e.g. one bending-twisting spring is between \mathbf{x}_{j-1} , \mathbf{x}_j , and \mathbf{x}_{j+1}). The stretching energy of each spring (Eq. 8) depends only on six DOFs (nodal coordinates of two nodes). For the stretching spring on edge e^j , these DOFs are \mathbf{x}_j and \mathbf{x}_{j+1} . The gradient vector $(\frac{\partial}{\partial \mathbf{q}} [\frac{1}{2} EA (\epsilon^j)^2 \|\bar{\mathbf{e}}^j\|])$ has only six non-zero terms

and the Hessian matrix $(\frac{\partial^2}{\partial \mathbf{q} \partial \mathbf{q}} [\frac{1}{2} EA (\epsilon^j)^2 \|\bar{\mathbf{e}}^j\|])$ has only 6×6 non-zero terms. The bending energy and the twisting energy of each spring (Eqs. 9 - 10) depend only on eleven DOFs, i.e. $\mathbf{x}_{j-1}, \theta^{j-1}, \mathbf{x}_j, \theta^j$, and \mathbf{x}_{j+1} in case of the spring located at \mathbf{x}_j in Figure 3(c). The gradient vector and the Hessian matrix of these two energies therefore have only eleven and 11×11 non-zero terms. The full expressions for the gradient and Hessian terms can be found in Bergou et al. (2008), Jawed et al. (2018), and Panetta et al. (2019); software implementation is also available in open-source repositories accompanying Jawed et al. (2014); Panetta et al. (2019); Choi et al. (2021).

The specific simulation studied in this paper requires the gradient of the external forces (Eq. 23). The external forces are expressed in Eqs. 11, 16, and 17. Their gradients with respect to the DOFs can be trivially obtained. Note that $\mathbb{J}_{ij}^{\text{ext}}$ is sparse. Since the expressions of all the Jacobian terms can be analytically evaluated and incorporated into the software, the simulation can use Euler-backward method. In comparison with Euler-forward method, Euler-backward method typically can converge at larger values of Δt and requires less computation time.

If the structure to be simulated is a single elastic rod (unlike a network of rods in this paper), the Jacobian is a banded matrix Bergou et al. (2010). In this paper, the Jacobian is not banded due to the presence of the joint node

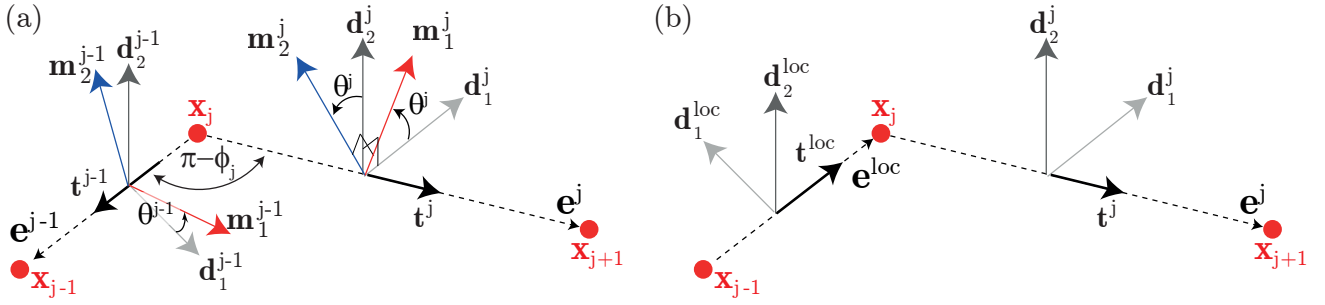


Figure 5. (a) Discrete bending and twisting energy is located at \mathbf{x}_j . Both the edges are pointing away from \mathbf{x}_j . (b) One of the edges (\mathbf{e}^{j-1} in this case) is flipped to slightly modify the kinematic representation. This representation can be used to compute the gradient and Hessian of the bending and twisting energies following analytical expressions available in the literature (Bergou et al. 2010).

\mathbf{x}_a in Figure 3(b). A second difference is related to the implementation of the gradient and Hessian of the bending and twisting energies. As in Figure 3, the expressions for gradient and Hessian in Bergou et al. (2010) assume that the tangent \mathbf{t}^{j-1} is pointing towards \mathbf{x}_j and the second tangent \mathbf{t}^j is pointing away from \mathbf{x}_j . Since this paper studies a network of rods, this assumption does not always hold. For example, as represented in Figure 5(a), we can have cases where both the tangents (\mathbf{t}^{j-1} and \mathbf{t}^j) point away from \mathbf{x}_j , the location of the bending and twisting spring. In this case, we can simply flip the first tangent ($\mathbf{t}^{loc} = -\mathbf{t}^{j-1}$ in Figure 5) and use $\{\mathbf{d}_1^{loc} = -\mathbf{d}_1^{j-1}, \mathbf{d}_2^{loc} = \mathbf{d}_2^j, \mathbf{t}^{loc} = -\mathbf{t}^{j-1}\}$ as the “local” reference frame on the edge $\mathbf{e}^{loc} = \mathbf{x}_j - \mathbf{x}_{j-1}$. The reference frame on the other edge \mathbf{e}^j remains unchanged to $\{\mathbf{d}_1^j, \mathbf{d}_2^j, \mathbf{t}^j\}$. Flipping the edge also implies that the twist angle on \mathbf{e}^{loc} in this local representation is $\theta^{loc} = -\theta^{j-1}$. This local representation in Figure 3(b) can be used to compute the gradient and Hessian of the bending and twisting energies at \mathbf{x}_j with respect to $\{\mathbf{x}_{j-1}, \theta^{loc}, \mathbf{x}_j, \theta^j, \mathbf{x}_{j+1}\}$ following the analytical expressions available in Bergou et al. (2010). Prior to including these gradient and Hessian terms in \mathbf{f} (Eq. 18) and \mathbb{J} (Eq. 20), we have to be mindful that $\frac{\partial}{\partial \theta^{j-1}}(\cdot) = -\frac{\partial}{\partial \theta^{loc}}(\cdot)$.

4.8 Physical parameters

The material and geometric parameters of the robot during experiments are listed as follows: Young’s modulus $E = 1.2 \times 10^6 \text{ N/m}^2$, Poisson’s ratio $\nu = 0.5$, density of soft tails 1000 kg/m^3 (this is used to compute m_i in Eq. 18), and cross-sectional radius of tails $r_0 = 3.2 \text{ mm}$. The length of each flagellum is $L_3 = 0.111 \text{ m}$, radius of the robot head is $a = 0.02 \text{ m}$, and the diameter of 3D-printed circular disc is $L_2 = 0.04 \text{ m}$. For the simulation data presented in this paper, time step is $\Delta t = 10^{-2} \text{ s}$ and the length of each edge on tails (in undeformed state) is $\|\bar{\mathbf{e}}^j\| = 4.11 \text{ mm}$. We performed convergence studies to ensure that the size of temporal and spatial discretization ($\Delta t, \|\bar{\mathbf{e}}^j\|$) has negligible effect on the simulation results. The parameters μ, C_1 , and C_2 will be fitted later in Section 5.3.

5 Results and discussion

Recall from Figure 1 that the motor embedded in the head generates a rotational speed, ω_T . As a result, the head and the tails rotate along opposite directions with rotational speeds of ω_h and ω_t such that $\omega_T = \omega_h + \omega_t$ (ω_T, ω_h , and ω_t are all non-negative values). The total rotational speed, ω_T , is considered as a control parameter in our study. The resulting rotation of the tails generate a propulsive force along the axial direction (see Figure 3). This propulsive force is used by the head and the tail to overcome the drag from the granular medium and the entire system moves forward with a speed v .

5.1 Threshold angular speed to move

When experiments were performed, it is found that there exists a threshold under which the robot stays still ($v = 0$) and above which it starts to move. This can be understood from the mechanics of granular materials. Such materials can behave as a solid but also flow as a fluid. A threshold angular speed is necessary to transform the medium from solid-like behavior to fluid-like flow. This threshold in our experiments is approximately $\omega_T \approx 50 \text{ rpm}$ and thus there are no data points at $\omega_T \lesssim 50 \text{ rpm}$ in the forthcoming discussion. In this regime of solid-like behavior, the tails and the head still rotate relative to one another; however, the whole robot does not change its location.

In this study, the maximum total angular speed is $\omega_T \approx 250 \text{ rpm}$ and the aforementioned regime ($\omega_T \approx 50$) is a relatively small part of the the overall parameter space. In the simulations, we use RFT that does not consider this threshold. Nonetheless, the simulation can capture the motion of the robot when $v > 0$. It is relatively straightforward to include this threshold in Algorithm 1 by using conditional statements to impose boundary conditions on the head. However, this will introduce new fitting parameters without much improvement in the overall predictive ability of the simulation.

5.2 Speed of the robot

We use the speed of the robot, v , along the axial direction as the primary performance metric of the robot. This parameter will be used in subsequent sections to study the effect of the total angular speed, ω_T , and the number of tails,

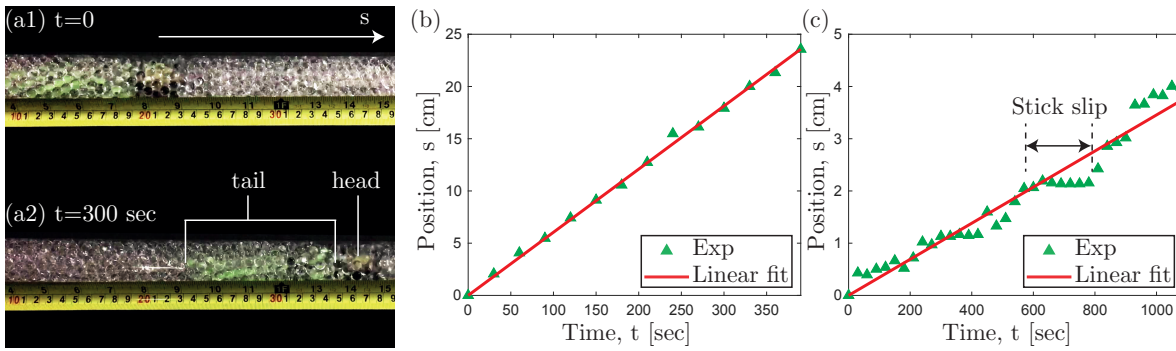


Figure 6. Position of the robot with time. (a1-a2) Snapshots from experiments showing the location of a robot with $n = 2$ and $\omega_{\text{total}} = 250$ rpm at time $t = 0$ and $t = 300$ s. (b) Position, s , of the same robot as a function of time, t . Solid line corresponds to the linear fit $s = vt$ where v is the speed. (c) Position vs. time of a robot with $n = 4$ and $\omega_{\text{total}} = 208$ rpm, where stick-slip dynamics is prominent.

n . The efficiency of the robot, η , will also be defined related with the speed, v .

During experiments, digital camera was used to capture videos of the motion of the robot. Figures 6(a1) and (a2) show two snapshots of a robot with $n = 2$ tails and total rotational speed $\omega_T = 250$ rpm at $t = 0$ and $t = 300$ sec. The green tails were marked with black markers and the black head was marked with bright yellow marker. Aided by the transparency of the granular medium and the markers on the robot, these videos were processed to extract the position of the robot, s , as a function of time. Figure 6(b) presents the position of the robot as a function of time. Closed triangles denote data from experiments and solid line represents a linear fit of the form $s = vt$. We observe that the robot moves at an almost constant velocity of $v \sim 0.6$ mm/s. This is expected from a solid body moving inside a medium governed by RFT.

On the other hand, Figure 6(c) shows the position of a robot with $n = 4$ tails and rotational speed $\omega_T = 208$ rpm. The motion of the robot is now qualitatively different from the one presented in Figure 6(b). The robot continuously moves forward in general but intermittently stays at the same position. This phenomenon is reminiscent of stick-slip – sudden motion that occurs when two multiple bodies are sliding past one another. At larger number of tails (e.g. $n = 4$ and $n = 5$), experimental observations indicate that the granular medium can get jammed (i.e. increase in viscosity) and the robot frequently gets stuck. Interestingly, our experiments (see Figure 6b) indicate the robot can resolve the jamming on its own through rotation (i.e. creating disturbance) for a few seconds. The periodic jamming and stick-slip cannot be captured by RFT and we do not include this behavior in our simulations. We focus only on robots with $n = 2$ and $n = 3$ tails that move at a constant speed with time. Nonetheless, this indicates room for expanding the theories for locomotion inside granular medium beyond RFT. Integrating such theories that describe the viscosity as a function of the robot configuration and time into Algorithm 1 should be a relatively trivial task.

5.3 Parameters fitting for simulations

We now move onto numerical simulations (details in Section 4) to model the locomotion and deformation of the robot. Recall from Eqs. 16 and 17 that C_1 and C_2 are fitting

parameters to account for the shape and surface roughness of the robot head. In addition, μ is the third fitting parameter standing for the dynamic viscosity of the granular medium. As detailed next, experimental data with a 2-tailed robot ($n = 2$) are used to estimate C_1 , C_2 , and μ . Simulations are performed with these parameters for the $n = 3$ case; simulation results are then compared against experiments for validation of the fitting process.

Figures 7(a) and (b) present the speed of the robot, v , and the rotational speed of the head, ω_h , respectively, as functions of the total rotational speed, ω_T . The data for $n = 2$ and $n = 3$ are shown in the figures. The data (v vs. ω_T and ω_h vs. ω_T) for $n = 2$ are used to obtain the best fit values of the fitting parameters: $C_1 = 2.420$, $C_2 = 0.039$, and $\mu = 6.828$. These parameters are then used in the numerical tool to simulate the locomotion of a robot with three tails. In Figure 7(a), speed vs. total rotational speed data show good agreement between experiments and simulations. Figure 7(b) shows the rotational speed of the head as a function of total rotational speed and we find that, in both experiments and simulations, a robot with $n = 3$ has a slightly larger head rotational speed than the one with $n = 2$.

The slight mismatch between the experimental results and simulation data can be partially attributed to the various assumptions made in the model. The fluid model assumes that the drag force exerted by the granular medium can be expressed using RFT. The structure model assumes that the tails are infinitesimally thin elastic rods. The drag force on the head is assumed to be linearly proportional to the velocity and the torque on the head is linearly proportional to its angular speed. In addition, invariably there are experimental errors, e.g. structural defects introduced during fabrication. Nonetheless, the reasonably good agreement between experiments and simulations support the validity of RFT in this case.

5.4 Speed vs. number of tails

A counter intuitive observation from Figure 7(a) is that, at a fixed value of rotational speed of the motor, ω_T , the robot with 2 tails moves faster than the one with 3 tails. Additionally, the speed vs. total rotational speed curve is nonlinear. All of these point to the large structural deformation and the strong coupling between the head and the tails.

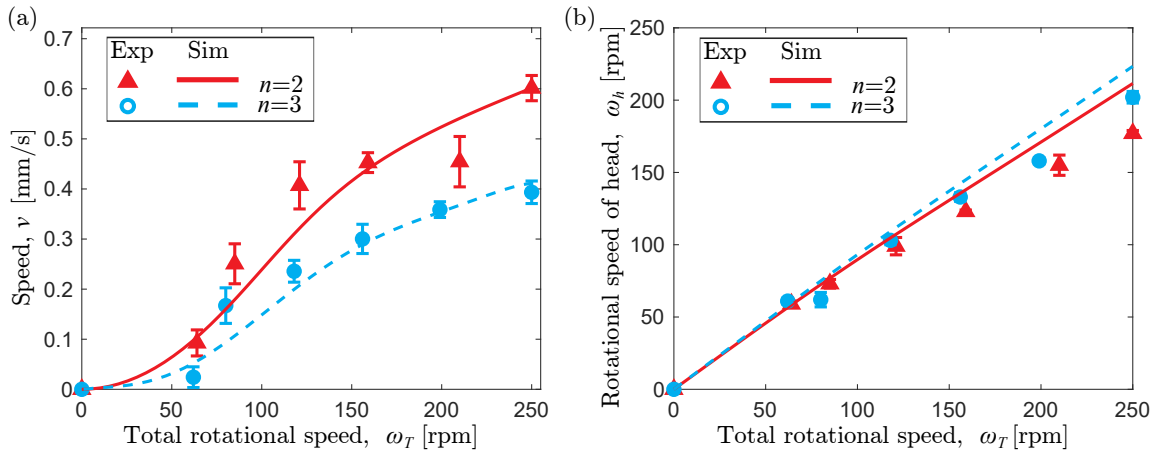


Figure 7. Comparison between experiment data and simulation results for the relationship between (a) total rotation speed of head and tail and robot moving speed; (b) total rotation speed of head and tail and rotation speed of head. The red triangles and blue circles with error bars are experiment data when the tail number is 2 and 3 respectively. The solid red line is the simulated outcome associated with the fitting parameters, C_h and μ whereas the dashed blue line represents the simulation result predicted by the same fitting parameters.

For a physical understanding of the dependence of speed on the number of tails, let us first note the rotational speed of the head for the two cases in Figure 7(b). As the number of tails, n , increases, the rotational speed of the head, ω_h , increases (at a fixed value of ω_T). Since $\omega_T = \omega_h + \omega_t$, this implies that the rotational speed of the tails, ω_t , decreases as the number of tails, n , increases. The propulsive force generated by each tail – let us denote this quantity as f_t – therefore also decreases. However, two additional factors to be considered to understand the overall speed, v , of the robot. First, the total propulsive force available is $n f_t$ and even though increasing n reduces f_t , it may (or may not) ultimately increase $n f_t$. Second, the total propulsive force is spent to overcome the drag on the head and the tail. As n increases, the amount of propulsive force spent on moving the tails forward also increases and the propulsive force budgeted for the head decreases. All of these factors above combined dictate the dependence between the robot speed and the number of tails.

In the experiments presented herein, the set of physical parameters are such that the speed decreases with the number of tails. However, this is not universally true for this system. For example, consider a robot with $C_2 \rightarrow \infty$ such that the head never rotates (i.e. $\omega_h = 0$). In that case, the rotational speed of the tail is always equal to the total rotation speed and f_t is a function of only ω_T (and not n). Then, the total propulsive force, $n f_t$, increases with n (assuming ω_T is fixed) and the speed of the robot is likely going to increase.

5.5 Efficiency

The efficiency, η , of the robot is defined as the ratio of propulsive force to propulsive torque. Since η is a non-dimensional quantity, we choose the radius of the head, a , as the length-scale. The expression for η is

$$\eta = \frac{|\mathbf{F}_h|}{|\mathbf{T}_h|} a = \frac{6\pi C_1 \mu a^2 v}{8\pi C_2 \mu a^3 \omega_h}, \quad (25)$$

where $|\cdot|$ denotes absolute value and expressions for \mathbf{F}_h and \mathbf{T}_h can be found in Eqs. 16 and 17, respectively.

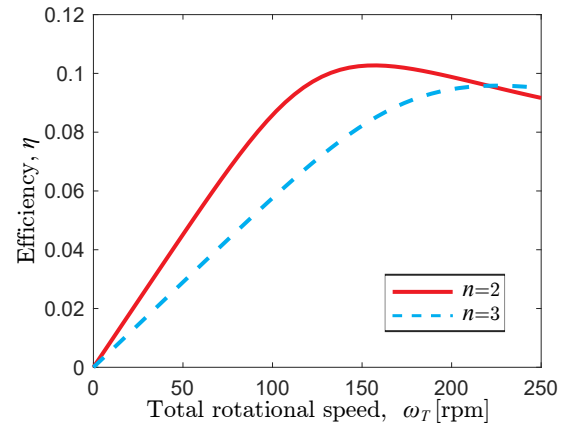


Figure 8. Variation of torque utilization efficiency versus the total rotational speed of robot predicted by our simulator.

The numerator can be understood as the drag force exerted by the medium on the robot while the denominator gives the total torque generated by the rotation of the motor. We use the simulator in Figure 8 to predict the variation of efficiency, η , with the rotational speed, ω_T , of the robot. The efficiency of a robot with $n = 2$ is non-monotonic and reaches the maximum at $\omega_T \approx 150$ rpm. At this optimal rotational speed, the robot moves the farthest per unit torque from the motor. Such clear presence of an optimal rotational speed in the operating range of the motor highlights the need for a numerical simulator that can be used as a design tool for the robot. Moreover, for $\omega_T \gtrsim 200$ rpm, the efficiency of a 2-tailed robot is greater than the one of a 3-tailed robot. Beyond $\omega_T \gtrsim 200$ rpm, the 3-tailed one performs better than the robot with 2 tails. These observations underline the high degree of nonlinearity in the functional dependence between the efficiency and the physical parameters (e.g. n and ω_T).

6 Conclusion

In this work, a discrete differential geometry-based simulation framework was introduced that models the

robot as a composition of Kirchhoff elastic rod. The robot is discretized into a system of mass-spring system, with discrete elastic (bending, twisting, stretching) energies associated with each spring. The total elastic energy of the robot is the sum of all the discrete elastic energies. Equations of motion are formulated that are simply statements of the following: at each DOF, the sum of elastic force (i.e. negative gradient of the elastic energy) and external force is equal to the lumped mass times acceleration of that DOF. The actuation of the robot (i.e. rotational speed of the motor) is represented by a time varying natural strain (specifically, the natural twist at the node representing the head). This approach allows us to simulate the shape of the robot in a fully implicit (Euler backward) manner.

The external force in this setup is the drag force exerted by the granular medium on the robotic structure. RFT – originally developed to model the hydrodynamics of low Reynolds fluid flow – was used to model the external force by the granular medium. This force can be seamlessly integrated into the simulation framework. Comparison between experiments and simulations showed that RFT is reasonably valid in case of the flagellated robot discussed here. However, when the number of tails is large (and the spacing between tails is small), “stick-slip” was observed and the underlying assumption behind RFT was no longer valid. In the future, the drag model of the granular medium can be improved to account for such behavior.

The simulation tool, supported by experiments, shed light on the highly nonlinear functional dependence between the performance of the robot (e.g. speed or efficiency) and the relevant physical parameters (e.g. the number of tails). Some counter-intuitive observations include the inverse relation between the speed and the number of tails of the robot in the representative setup. The non-monotonic dependence of efficiency on the rotational speed of the motor highlighted the necessity of a design tool for optimal control of the robot. The computational speed of the simulator can be exploited to run parametric studies and identify the optimal design and control of this class of robots that can be represented by stick figures.

7 Funding

This work was supported by the Henry Samueli School of Engineering and Applied Science, University of California and the National Science Foundation (Award # IIS-1925360).

References

- Alexander, R.M., 2003. Principles of animal locomotion. Princeton University Press.
- Audoly, B., Pomeau, Y., 2000. Elasticity and geometry, in: Peyresq Lectures on Nonlinear Phenomena. World Scientific, pp. 1–35.
- Baek, C., Sageman-Furnas, A.O., Jawed, M.K., Reis, P.M., 2018. Form finding in elastic gridshells. *Proceedings of the National Academy of Sciences* 115, 75–80.
- Bartlett, M.D., Kazem, N., Powell-Palm, M.J., Huang, X., Sun, W., Malen, J.A., Majidi, C., 2017. High thermal conductivity in soft elastomers with elongated liquid metal inclusions. *Proceedings of the National Academy of Sciences*, 201616377.
- Bergou, M., Audoly, B., Vouga, E., Wardetzky, M., Grinspun, E., 2010. Discrete viscous threads, in: *ACM Transactions on Graphics*, ACM. p. 116.
- Bergou, M., Wardetzky, M., Robinson, S., Audoly, B., Grinspun, E., 2008. Discrete elastic rods. *ACM transactions on graphics (TOG)* 27, 63.
- Biewener, A.A., 1990. Biomechanics of mammalian terrestrial locomotion. *Science* 250, 1097–1103.
- Choi, A., Tong, D., Jawed, M.K., Joo, J., 2021. Implicit contact model for discrete elastic rods in knot tying. *Journal of Applied Mechanics*, 1–13.
- Conte, J., Modarres-Sadeghi, Y., Watts, M., Hover, F.S., Triantafyllou, M.S., 2010. A fast-starting mechanical fish that accelerates at 40 ms⁻². *Bioinspiration & biomimetics* 5, 035004.
- Dickinson, M.H., Farley, C.T., Full, R.J., Koehl, M., Kram, R., Lehman, S., 2000. How animals move: an integrative view. *science* 288, 100–106.
- Ding, Y., Sharpe, S.S., Masse, A., Goldman, D.I., 2012. Mechanics of undulatory swimming in a frictional fluid. *PLoS computational biology* 8, e1002810.
- Forghani, M., Huang, W., Jawed, M.K., 2021. Control of uniflagellar soft robots at low reynolds number using buckling instability. *Journal of Dynamic Systems, Measurement, and Control* 143, 061004.
- Gray, J., 1968. Animal locomotion. Weidenfeld & Nicolson.
- Gray, J., Hancock, G., 1955. The propulsion of sea-urchin spermatozoa. *Journal of Experimental Biology* 32, 802–814.
- Hu, D.L., Nirody, J., Scott, T., Shelley, M.J., 2009. The mechanics of slithering locomotion. *Proceedings of the National Academy of Sciences* 106, 10081–10085.
- Jawed, M., Reis, P.M., 2017. Dynamics of a flexible helical filament rotating in a viscous fluid near a rigid boundary. *Physical Review Fluids* 2, 034101.
- Jawed, M.K., Da, F., Joo, J., Grinspun, E., Reis, P.M., 2014. Coiling of elastic rods on rigid substrates. *Proceedings of the National Academy of Sciences* 111, 14663–14668.
- Jawed, M.K., Khouri, N., Da, F., Grinspun, E., Reis, P.M., 2015. Propulsion and instability of a flexible helical rod rotating in a viscous fluid. *Physical review letters* 115, 168101.
- Jawed, M.K., Novelia, A., O’Reilly, O.M., 2018. A Primer on the Kinematics of Discrete Elastic Rods. Springer.
- Jawed, M.K., Reis, P.M., 2016. Deformation of a soft helical filament in an axial flow at low reynolds number. *Soft matter* 12, 1898–1905.
- Johnson, R., Brokaw, C., 1979. Flagellar hydrodynamics. a comparison between resistive-force theory and slender-body theory. *Biophysical journal* 25, 113–127.
- Kim, S., Laschi, C., Trimmer, B., 2013. Soft robotics: a bioinspired evolution in robotics. *Trends in biotechnology* 31, 287–294.
- Kirchhoff, G., 1859. Über das gleichgewicht und die bewegung eines unendlich dunnen elastischen stabes. *J. Reine Angew. Math.* 56, 285–313.
- Laschi, C., Cianchetti, M., Mazzolai, B., Margheri, L., Follador, M., Dario, P., 2012. Soft robot arm inspired by the octopus. *Advanced Robotics* 26, 709–727.
- Lauga, E., 2011. Life around the scallop theorem. *Soft Matter* 7, 3060–3065.

- Lauga, E., Powers, T.R., 2009. The hydrodynamics of swimming microorganisms. *Reports on Progress in Physics* 72, 096601.
- Lazarus, A., Miller, J.T., Metlitz, M.M., Reis, P.M., 2013. Contorting a heavy and naturally curved elastic rod. *Soft Matter* 9, 8274–8281.
- Licht, S., Polidoro, V., Flores, M., Hover, F.S., Triantafyllou, M.S., 2004. Design and projected performance of a flapping foil auv. *IEEE Journal of oceanic engineering* 29, 786–794.
- Lighthill, J., 1976. Flagellar hydrodynamics. *SIAM review* 18, 161–230.
- Lin, H.T., Leisk, G.G., Trimmer, B., 2011. Goqbot: a caterpillar-inspired soft-bodied rolling robot. *Bioinspiration & biomimetics* 6, 026007.
- Macnab, R.M., Ornston, M.K., 1977. Normal-to-curly flagellar transitions and their role in bacterial tumbling. stabilization of an alternative quaternary structure by mechanical force. *Journal of molecular biology* 112, 1–30.
- Majidi, C., Shepherd, R.F., Kramer, R.K., Whitesides, G.M., Wood, R.J., 2013. Influence of surface traction on soft robot undulation. *The International Journal of Robotics Research* 32, 1577–1584.
- Maladen, R.D., Ding, Y., Li, C., Goldman, D.I., 2009. Undulatory swimming in sand: subsurface locomotion of the sandfish lizard. *science* 325, 314–318.
- Maladen, R.D., Ding, Y., Umbanhowar, P.B., Goldman, D.I., 2011a. Undulatory swimming in sand: experimental and simulation studies of a robotic sandfish. *The International Journal of Robotics Research* 30, 793–805.
- Maladen, R.D., Ding, Y., Umbanhowar, P.B., Kamor, A., Goldman, D.I., 2011b. Mechanical models of sandfish locomotion reveal principles of high performance subsurface sand-swimming. *Journal of The Royal Society Interface* 8, 1332–1345.
- Miller, J., Lazarus, A., Audoly, B., Reis, P.M., 2014. Shapes of a suspended curly hair. *Physical review letters* 112, 068103.
- Panetta, J., Konaković-Luković, M., Isvoranu, F., Bouleau, E., Pauly, M., 2019. X-shells: A new class of deployable beam structures. *ACM Transactions on Graphics (TOG)* 38, 1–15.
- Pérez, J., Thomaszewski, B., Coros, S., Bickel, B., Canabal, J.A., Sumner, R., Otaduy, M.A., 2015. Design and fabrication of flexible rod meshes. *ACM Transactions on Graphics* 34, 138.
- Renda, F., Giorgio-Serchi, F., Boyer, F., Laschi, C., Dias, J., Seneviratne, L., 2018. A unified multi-soft-body dynamic model for underwater soft robots. *The International Journal of Robotics Research* 37, 648–666.
- Rodenborn, B., Chen, C.H., Swinney, H.L., Liu, B., Zhang, H., 2013. Propulsion of microorganisms by a helical flagellum. *Proceedings of the National Academy of Sciences* 110, E338–E347.
- Rus, D., Tolley, M.T., 2015. Design, fabrication and control of soft robots. *Nature* 521, 467.
- Saimek, S., Li, P.Y., 2004. Motion planning and control of a swimming machine. *The International Journal of Robotics Research* 23, 27–53.
- Scaramuzza, D., Siegwart, R., Martinelli, A., 2009. The international journal of robotics research. *The International Journal of Robotics Research* 28, 149–171.
- Schenk, O., Gärtner, K., 2002. Solving unsymmetric sparse systems of linear equations with pardiso, in: *International Conference on Computational Science*, Springer. pp. 355–363.
- Shepherd, R.F., Ilievski, F., Choi, W., Morin, S.A., Stokes, A.A., Mazzeo, A.D., Chen, X., Wang, M., Whitesides, G.M., 2011. Multigait soft robot. *Proceedings of the national academy of sciences* 108, 20400–20403.
- Son, K., Guasto, J.S., Stocker, R., 2013. Bacteria can exploit a flagellar buckling instability to change direction. *Nature physics* 9, 494.
- Taylor, G.K., Nudds, R.L., Thomas, A.L., 2003. Flying and swimming animals cruise at a strouhal number tuned for high power efficiency. *Nature* 425, 707.
- Texier, B.D., Ibarra, A., Melo, F., 2017. Helical locomotion in a granular medium. *Physical review letters* 119, 068003.
- Thawani, A., Tirumkudulu, M.S., 2018. Trajectory of a model bacterium. *Journal of Fluid Mechanics* 835, 252–270.
- Tolley, M.T., Shepherd, R.F., Mosadegh, B., Galloway, K.C., Wehner, M., Karpelson, M., Wood, R.J., Whitesides, G.M., 2014. A resilient, untethered soft robot. *Soft robotics* 1, 213–223.
- Yu, J., Ding, R., Yang, Q., Tan, M., Wang, W., Zhang, J., 2012. On a bio-inspired amphibious robot capable of multimodal motion. *IEEE/ASME Transactions On Mechatronics* 17, 847–856.
- Zhang, T., Goldman, D.I., 2014. The effectiveness of resistive force theory in granular locomotion. *Physics of Fluids* 26, 101308.